Nanoscale

PAPER

View Article Online
View Journal | View Issue

Cite this: *Nanoscale*, 2026, **18**, 3419

Phase-engineered bismuth-rich oxybromides ($Bi_xO_yBr_z$) for visible-light photocatalytic degradation of emerging pollutants and harmful algal blooms

A. Anjitha, [a] Safa Leen,[a] K. V. Ajayan, [b] Anna Zielińska-Jurek [c] and Kishore Sridharan *[a,c]

Non-stoichiometric bismuth-rich bismuth oxybromides ($Bi_xO_yBr_z$) have attracted significant attention due to their excellent stability, tunable band structure, visible light responsiveness, and unique 2D layered morphology. In this study, a modified hydrolysis method was adopted to synthesize a BiOBr precursor using an elevated concentration of the Bi^{3+} precursor. Subsequent calcination of the as-prepared BiOBr precursor at varying temperatures induced phase transformation into $Bi_{24}O_{31}Br_{10}$, $Bi_4O_5Br_2$, Bi_5O_7Br, and $Bi_{12}O_{17}Br_2$, as confirmed by XRD analysis. Morphological characterization *via* FESEM and TEM revealed the retention of layered 2D plate-like structures, while XPS analysis further corroborated the phase transitions by identifying changes in surface composition and chemical states. The photocatalytic activities of these phase-engineered $Bi_xO_yBr_z$ materials were evaluated through the degradation of methylene blue dye and acetaminophen under visible-light irradiation. Notably, $Bi_{12}O_{17}Br_2$ demonstrated superior photocatalytic performance and was further investigated for its efficacy in degrading *Microcystis aeruginosa* algal cells. The enhanced activity of $Bi_{12}O_{17}Br_2$ is attributed to improved generation of reactive oxygen species and reduced electron–hole pair recombination, facilitated by its inherent ability to generate an internal static electric field. This work highlights a cost-effective strategy for designing $Bi_xO_yBr_z$ photocatalysts with phase-dependent activity toward both chemical and biological pollutants of emerging concern.

Received 29th November 2025,
Accepted 29th December 2025

DOI: 10.1039/d5nr05038c

rsc.li/nanoscale

1. Introduction

Water pollution, exacerbated by rapid urbanization, industrial growth, and increasing population, poses a severe threat to environmental sustainability and public health. The release of industrial effluents, agricultural runoff, and untreated domestic wastewater has led to the accumulation of various contaminants, including synthetic dyes, pharmaceutical residues, and harmful biological pollutants.[1,2] Among these, methylene blue dye (MBD), extensively used in the textile, paper, leather, and biomedical industries, is particularly concerning due to its high solubility and chemical stability. Its persistence in aquatic environments can lead to ecological imbalances, toxicity in aquatic organisms, and potential carcinogenic effects in humans. Similarly, pharmaceutical contaminants such as paracetamol (acetaminophen, AMP) frequently appear in wastewater due to their incomplete removal by conventional treatment systems.[3] Even at trace concentrations, these pollutants can disrupt aquatic ecosystems, interfere with endocrine functions in marine organisms, and contribute to the proliferation of antibiotic-resistant bacteria. The continuous presence of such contaminants underscores the need for efficient degradation strategies to mitigate their detrimental effects.[4]

Another critical environmental challenge is the proliferation of harmful algal blooms, particularly those caused by *Microcystis aeruginosa* (MA). Excessive nutrient influx from fertilizers and untreated wastewater accelerates eutrophication, fostering the rapid expansion of cyanobacterial populations. These blooms not only deplete dissolved oxygen levels, creating inhospitable conditions for aquatic life, but also release potent toxins such as microcystin-LR. Exposure to microcystin-LR has been associated with severe health risks, including liver damage and an increased likelihood of colon cancer, highlighting the urgent need for effective remediation strategies.[5,6] Given the limitations of conventional wastewater treatment methods in effectively addressing these contami-

[a]*Department of Nanoscience and Technology, University of Calicut, P.O. Calicut University, Kerala 673635, India*
[b]*Department of Botany, University of Calicut, P.O. Calicut University, Kerala 673635, India*
[c]*Department of Process Engineering and Chemical Technology, Faculty of Chemistry, Gdansk University of Technology, 80-233 Gdansk, Poland.*
E-mail: sridharankishore@uoc.ac.in, kishore.sridharan@pg.edu.pl

nants, the development of advanced treatment technologies has become imperative.

Among emerging solutions, advanced oxidation processes (AOPs) have gained prominence due to their ability to generate highly reactive oxygen species (ROS), such as hydroxyl radicals ($^{\bullet}OH$) and superoxide anions ($^{\bullet}O_2^-$). These reactive species facilitate the degradation of complex pollutants, breaking them down into harmless byproducts like CO_2, H_2O, and inorganic ions. Among various AOPs, semiconductor-based photocatalysis stands out as a promising, cost-effective, and environmentally sustainable approach. This method utilizes UV–visible light to excite electrons in a semiconductor catalyst, such as titanium dioxide (TiO_2), generating electron–hole pairs that drive redox reactions. In aqueous systems, these reactive species promote the degradation of organic pollutants through oxidation and reduction processes, leading to their complete mineralization. The effectiveness of photocatalysis in breaking down persistent contaminants, including synthetic dyes, pharmaceuticals, and harmful algal toxins, underscores its potential as a transformative solution for modern wastewater treatment and environmental management.

Despite the extensive research on TiO_2 as a photocatalyst, its practical application remains restricted due to its limited activity under UV light, which constitutes only about 5% of the solar spectrum.[7] To enhance its visible-light-driven performance – crucial given that visible light makes up approximately 43% of solar energy – various modification strategies have been explored, including doping with metals like silver and bismuth, as well as the incorporation of polymer-based materials.[8–10] These modifications have significantly improved its solar energy utilization for environmental remediation applications. In this context, two-dimensional (2D) semiconductor photocatalysts have garnered increasing attention over their zero-dimensional (0D) and one-dimensional (1D) counterparts due to their distinct structural and electronic advantages. Their ultrathin morphology offers a large surface area and shorter charge transport pathways, which help reduce charge recombination and enhance photocatalytic efficiency. Additionally, their superior light absorption, strong pollutant adsorption, and tunable electronic properties can be further optimized through heterostructure engineering, making them highly adaptable for energy and environmental applications. Among various 2D semiconductors, bismuth oxyhalides (BiOX, where X = F, Cl, Br, and I) have been widely recognized for their unique properties. These materials possess layered crystal structures, tunable bandgaps, excellent chemical stability, and efficient charge separation capabilities. Structurally, BiOX adopts a tetragonal matlockite-type arrangement, consisting of alternating [X–Bi–O–Bi–X] layers held together by weak van der Waals interactions along the *c*-axis. This distinctive structure contributes to their high photocatalytic activity, making them promising candidates for advanced photocatalytic applications under visible light.[11]

However, conventional BiOX photocatalysts exhibit relatively positive conduction band (CB) positions, which may limit their efficiency in driving reduction reactions. To address this limitation, researchers have synthesized non-stoichiometric bismuth oxyhalides, commonly referred to as bismuth-rich bismuth oxyhalides ($Bi_xO_yX_z$, where X = Cl, Br, I).[11–13] These materials exhibit more negative CB positions, thereby enhancing their potential to facilitate critical photocatalytic reactions, including CO_2 reduction, H_2 evolution and N_2 fixation. Additionally, their higher valence band (VB) positions relative to the $H_2O/^{\bullet}OH$ potential enable efficient oxidation reactions, making them highly suitable for sustainable environmental remediation and energy conversion applications.[14,15]

Since the initial report on bismuth-rich Bi_3O_4Cl in 2006,[16] numerous $Bi_xO_yX_z$ compounds, such as Bi_3O_4Br, $Bi_{12}O_{17}Br_2$, Bi_5O_7Br, and Bi_5O_7I, have been synthesized.[17] These materials exhibit bandgap energies ranging from 2.0 to 3.6 eV, allowing them to efficiently absorb both UV and visible light. Various synthesis approaches, including hydrothermal, solvothermal, and calcination-based methods, have been employed to fine-tune their composition, consequently modifying their photocatalytic properties. Specifically, the phase transformation studies revealed that bismuth oxyiodides (*e.g.*, BiOI, $Bi_4O_5I_2$, Bi_5O_7I, and $Bi_7O_9I_3$) synthesized *via* dehalogenation strategies, especially by controlled calcination, exhibit enhanced photocatalytic activity,[4,18,19] whereas most $Bi_xO_yBr_z$ materials have relied on hydrothermal or solvothermal methods for synthesis.[20–25] While effective, these methods are typically time-consuming and require high pressures but yield relatively small amounts of $Bi_xO_yBr_z$ photocatalysts.[26] In contrast, our study demonstrates a straightforward calcination-based approach for synthesizing phase-controlled Bi-rich oxybromides from a simple BiOBr precursor synthesized using a simple hydrolysis method.[27] This route enables tuning the physio-chemical properties of the photocatalyst through temperature-induced phase transitions, which remains relatively less explored in the current literature.

In this study, we synthesized a series of $Bi_xO_yBr_z$ photocatalysts using a modified hydrolysis method, followed by calcination of the resulting precipitate at temperatures ranging from 200 °C to 500 °C. This approach yielded $Bi_{24}O_{31}Br_{10}$, $Bi_4O_5Br_2$, Bi_5O_7Br, and $Bi_{12}O_{17}Br_2$ photocatalysts. The photocatalytic activity of these materials was evaluated by assessing their efficiency towards the degradation of MBD and AMP under visible light exposure. The most effective photocatalyst, $Bi_{12}O_{17}Br_2$, was further tested for its ability to degrade MA collected from natural pond water. While previous research has primarily focused on solvothermal or hydrothermal synthesis, this study presents a novel approach by employing a simple hydrolysis method followed by controlled calcination, which remains largely unexplored. Additionally, to the best of our knowledge, this is the first study investigating the photocatalytic degradation of MA using pristine $Bi_{12}O_{17}Br_2$, highlighting its potential for addressing emerging environmental contaminants. Our findings demonstrate that $Bi_xO_yBr_z$ are excellent photocatalysts with the flexibility to modify their band structure and light absorption properties, making them highly effective in mitigating environmental pollutants. These

advancements further underscore the growing potential of $Bi_xO_yX_z$ for sustainable environmental remediation.

2. Experimental

2.1. Materials

Analytical grade chemicals such as bismuth nitrate pentahydrate ($Bi(NO_3)_3{\cdot}5H_2O$), potassium bromide (KBr), and ethanol were procured from Merck and were used without any purification. Also, acetaminophen ($C_8H_9NO_2$) and methylene blue dye of the highest purity purchased from LOBA Chemie Laboratories and Sigma Aldrich, respectively, were utilized as received. High purity deionized (DI) water (resistivity ~18.2 MΩ cm) was used throughout the experiments.

2.2. Synthesis of $Bi_xO_yBr_z$ photocatalysts through hydrolysis followed by calcination

BiOBr precursor powder was first synthesized through a controlled hydrolysis method. First, 0.0268 g of KBr (0.02 M) was dissolved in 15 mL of DI water and heated to 90 °C under continuous stirring. In parallel, 0.97 g of $Bi(NO_3)_3{\cdot}5H_2O$ (0.1 M) was dispersed in 20 mL of ethanol to prevent premature hydrolysis and ensure controlled nucleation upon mixing with Br^- solution. The Bi^{3+}/Br^- molar ratio was selected to maintain a slight excess of Bi^{3+}, which helps prevent the formation of secondary oxybromide impurities. Once the KBr solution reached 90 °C, the Bi^{3+} ethanol suspension was slowly added dropwise over ~5 min. Upon addition, the reaction mixture turned turbid, and white precipitates formed through the reaction of Bi^{3+} and Br^- and hydrolyzed hydroxyl species. During hydrolysis, the pH of the reaction mixture stabilized at ~6.2, which is within the optimal range for BiOBr nucleation. After mixing, the suspension was maintained at 90 °C for an additional 30 min, allowing partial evaporation of solvent and growth of precursor particles. The resulting precipitate was collected by centrifugation and washed three times each with DI water and ethanol to remove residual ions and nitrate species. White precursor powder was obtained by drying the precipitate in an oven at 100 °C for 12 h. To obtain $Bi_xO_yBr_z$ photocatalysts with tailored crystallinity and oxygen defect concentrations, the BiOBr precursor was calcined at different temperatures. Samples designated as BC2, BC3, BC4, and BC5 were produced by calcining the precursor at 200 °C, 350 °C, 400 °C, and 500 °C, respectively, for 2 h, with a heating rate of 10 °C min^{-1}. The temperatures were chosen to progressively induce partial decomposition and oxygen defect formation while avoiding transition to Bi_2O_3 at higher temperatures. Details corresponding to the characterization of the samples are presented in Text S1 (SI).

2.3. Visible light driven photocatalytic degradation of methylene blue and acetaminophen

The photodegradation efficiencies of the $Bi_xO_yBr_z$ photocatalysts were assessed by studying the degradation of MBD and AMP. The studies were conducted under visible light by employing a Luzchem Xenon photoreactor fitted with a 300 W Xenon lamp. Typically, the experiments were conducted by dispersing 1 g L^{-1} of the synthesized photocatalysts in separate aqueous solutions of 10 ppm MBD and AMP, respectively. The suspension was stirred for 30 min in the dark before being exposed to light for establishing the adsorption–desorption equilibrium between the catalyst and pollutant molecules. Later, the photocatalysis reaction was initiated by irradiating light and aliquots were collected regularly at fixed intervals. In the case of MBD degradation, the photocatalyst was removed from the aliquots *via* double centrifugation at 8000 rpm, whereas for AC degradation, the aliquots underwent additional filtration using a 0.22 μm PTFE syringe filter following centrifugation. The concentration variations of AC and its degradation byproducts were analyzed with a high-performance liquid chromatography system (HPLC-LC/MS, Agilent 6120 MSD), loaded with a UV–visible diode array detector. The separation was carried out using a C18 column, with detection set at 243 nm. The mobile phase consisted of 75% acetonitrile and 25% water, flowing at a rate of 0.1 mL min^{-1} for a duration of 10 min.[28] The concentration changes of both MBD and AMP were also monitored with the help of a UV–visible spectrophotometer. For ensuring reproducibility, all the experiments were carried out in triplicate and the efficiency of the photocatalyst was ascertained with the equation

$$\text{Efficiency}\,(\%) = \left[\frac{C_0 - C}{C_0}\right] \times 100$$

where C_0 and C denote the initial and irradiation time-dependent concentrations of the pollutants. Experimental details pertaining to the visible-light driven photodegradation of MA algal cells are presented in Text S2 (SI).

3. Results and discussion

3.1. Structural, chemical, and morphological characterization

The crystal structure and phase composition of the synthesized samples were analyzed using powder XRD. Phase identification and structural analysis were performed using X'Pert HighScore Plus software. The XRD pattern of the precipitate obtained through the hydrolysis method is shown in Fig. S1 (SI).

The majority of the diffraction peaks of the precipitate primarily correspond to the pure tetragonal phase of BiOBr (JCPDS card # 73-2061), with some reflections matching $Bi_xO_yBr_z$. As illustrated in Fig. 1, the XRD pattern of BC2 formed by calcining the pre-synthesized precipitate at 200 °C predominantly exhibited peaks associated with monoclinic $Bi_{24}O_{31}Br_{10}$ (JCPDS card # 75-0888) with a few peaks of tetragonal BiOBr (JCPDS card # 73-2061). Notably, characteristic peaks at 2θ = 10.52° and 31.82°, corresponding to the (10−2) and (11−7) planes of $Bi_{24}O_{31}Br_{10}$, respectively, overlap with the (001) and (012) planes of BiOBr, are representative of the phase transition from BiOBr to $Bi_xO_yBr_z$.

While the pre-synthesized precipitate was calcined at temperatures of 350 °C, 400 °C and 500 °C, a progressive shift in

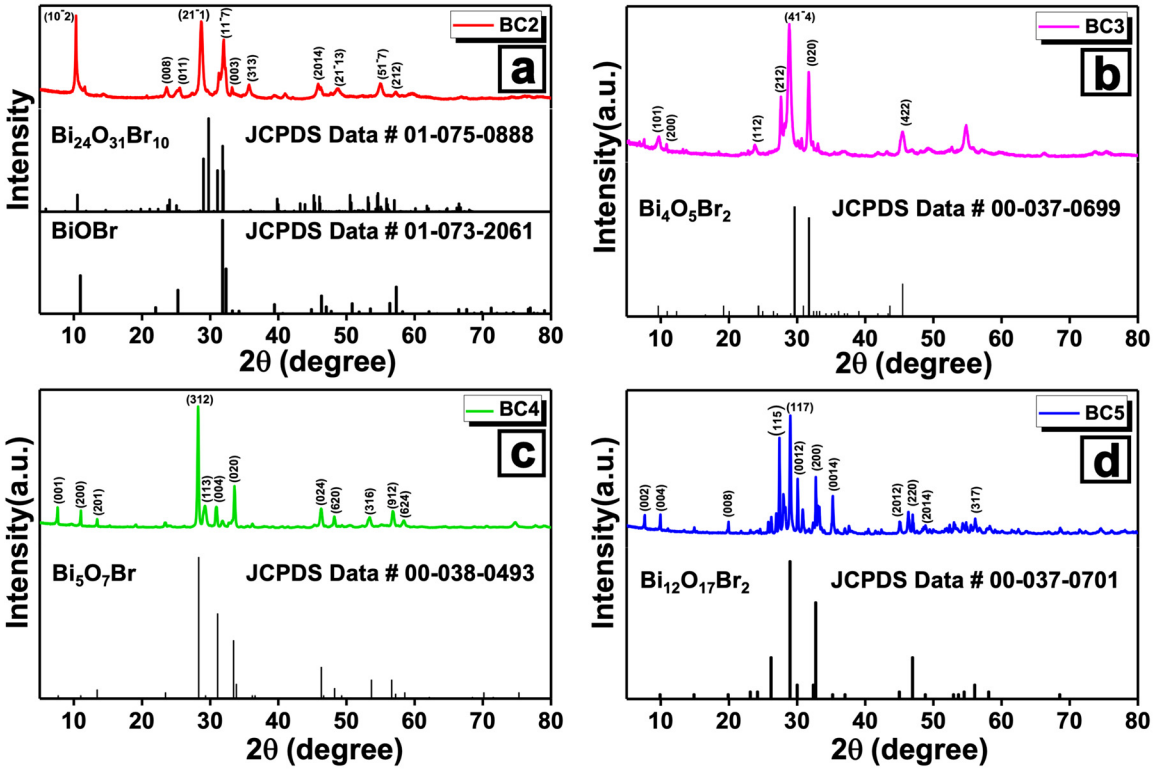

Fig. 1 XRD patterns of the synthesized photocatalysts: (a) BC2, (b) BC3, (c) BC4, and (d) BC5.

the XRD peaks toward lower angles is observed, indicating phase transitions at every step leading to the formation of $Bi_4O_5Br_2$, Bi_5O_7Br and $Bi_{12}O_{17}Br_2$, respectively, due to bromine loss.[29] The XRD patterns of BC3 and BC4 obtained by calcining the precipitate at 350 °C and 400 °C correspond to monoclinic $Bi_4O_5Br_2$ (JCPDS card # 37-0699) and monoclinic Bi_5O_7Br (JCPDS card # 38-0493), respectively, as shown in Fig. 1b and c. Similarly, the XRD pattern of BC5 obtained after calcining the precipitate at 500 °C indicated the transformation of BiOBr into tetragonal phase $Bi_{12}O_{17}Br_2$ and perfectly matched the standard XRD data of tetragonal $Bi_{12}O_{17}Br_2$ (JCPDS card # 37-0701).

The average crystallite size and structural defects, including dislocation density and microstrain, were determined from XRD data using both the Scherrer equation and the Williamson–Hall (W–H) plot (see Fig. S2), with the results summarized in Table S1 (SI).[30] It was observed that crystallite sizes calculated using both methods were increased with rising temperature,[31] but a variation in crystallite size values was observed between the two methods. This difference arises because the Scherrer equation assumes isotropic spherical crystallites and neglects strain, whereas the W–H method considers both crystallite size and lattice strain contributions.[32] Samples with smaller crystallite sizes exhibited a higher number of lattice defects, where bromine atoms at these defect sites experienced increased energy, potentially acting as nucleation centers for phase transitions at elevated temperatures.[33] These phase transformations typically occur through thermal decomposition, where bromine sublimation and evaporation lead to structural modifications, as described by the following reactions:[4,34]

$$8BiOBr + O_2 \rightarrow 2Bi_4O_5Br_2 + 2Br_2 \quad (1)$$

$$5BiOBr + O_2 \rightarrow Bi_5O_7Br + 2Br_2 \quad (2)$$

$$24BiOBr + 5O_2 \rightarrow 2Bi_{12}O_{17}Br_2 + 10Br_2 \quad (3)$$

To further investigate the surface composition and chemical states of the synthesized photocatalysts, XPS was conducted. The survey spectra of BC2, BC3, BC4, and BC5 in Fig. 2a confirm the presence of Bi, O, Br, and C, with a minor C 1s peak at 284.8 eV, likely due to adventitious carbon contamination.[35] The high-resolution Bi 4f spectra in Fig. 2b show peaks for Bi $4f_{5/2}$ at approximately 164.38 eV, 164.08 eV, 163.98 eV, and 163.98 eV for BC2, BC3, BC4, and BC5, respectively. The Bi $4f_{7/2}$ peaks at 159.02 eV, 158.78 eV, 158.68 eV, and 158.98 eV confirm the presence of Bi^{3+} in all the synthesized photocatalysts.

The O 1s spectra in Fig. 2c reveal peaks at 532.04, 530.58, 531.24, and 530.7 eV, which can be attributed to surface chemisorbed hydroxyl (–OH) groups, while a peak at 529 eV corresponds to lattice oxygen associated with Bi–O bonds. The Br 3d spectra in Fig. 2d show Br $3d_{5/2}$ peaks at 68.26, 68.19, 68.09, and 68.34 eV, along with Br $3d_{3/2}$ peaks at 69.36, 69.32, 69.19, and 69.43 eV, confirming the presence of Br^- in the Bi–O–Br framework of the $Bi_xO_yBr_z$ photocatalysts.[35–37] Notably, a

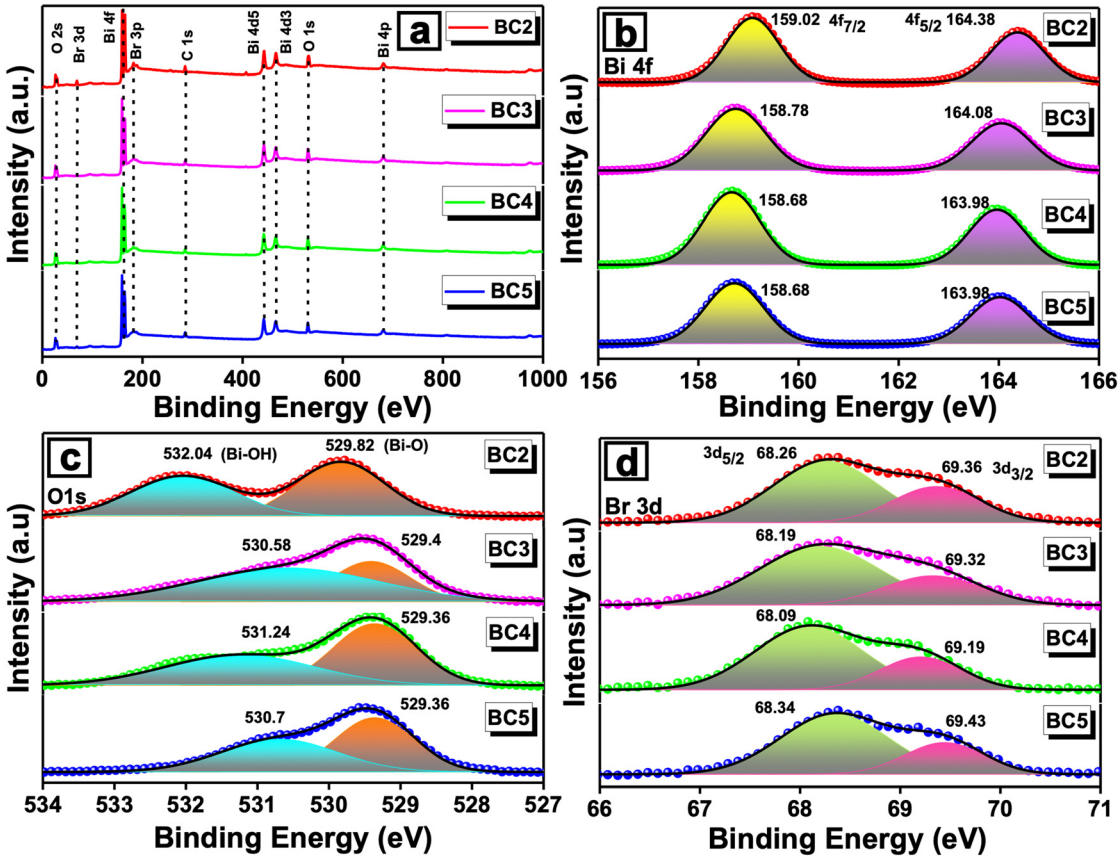

Fig. 2 XPS analysis of the BC2, BC3, BC4 and BC5 photocatalysts: (a) survey spectra, and deconvoluted spectra of (b) Bi 4f, (c) O 1s, and (d) Br 3d.

significant decrease in Br 3d peak intensity is observed for BC5, indicating a deviation from the expected surface stoichiometry. This reduction is likely due to partial volatilization of bromine during high-temperature calcination, which can generate bromine vacancies and related surface defects. Such behaviour has been previously reported in thermally treated bismuth oxyhalides, where elevated temperatures promote Br_2 release.[38] These findings suggest that high-temperature processing strongly influences the surface bromine environment in BC5 ($Bi_{12}O_{17}Br_2$).

The morphologies of all the $Bi_xO_yBr_z$ photocatalysts obtained after calcination at various temperatures were analyzed using FESEM. Notably, the typical 2D plate-like morphology of the BiOBr precipitate (Fig. S3a and b) was found to be intact despite the calcination-led phase transformations into various $Bi_xO_yBr_z$ photocatalysts. As observed from Fig. S3c and d, the FESEM micrographs of BC2 formed at 200 °C reveal the 2D nanoplates with an average thickness of ≤11 nm and loosely agglomerated structures. Particles of BC3 with a 2D nanoplate morphology formed at 350 °C displayed a non-uniform size distribution with varying thicknesses (Fig. S3e and S3f). Nanoplates with an average thickness of ~13 nm were observed from the FESEM micrographs (Fig. S3g and S3h) of BC4, indicating that increasing the calcination temperature to 400 °C resulted in significant grain growth. As observed from Fig. 3, the

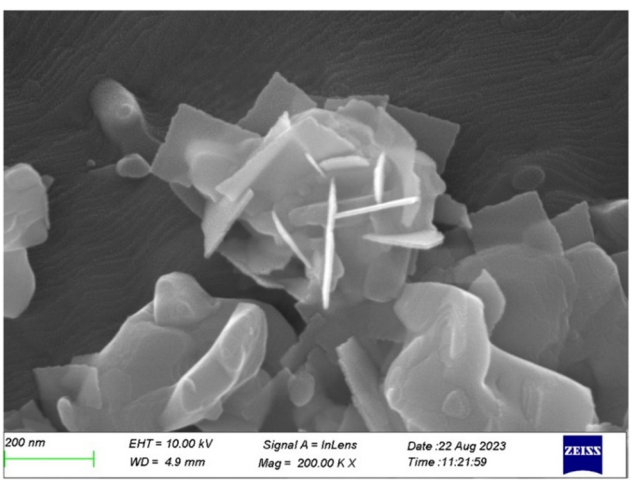

Fig. 3 FESEM micrograph depicting the 2D nanoplate-like morphology of the $Bi_{12}O_{17}Br_2$ (BC5) photocatalyst.

calcination at 500 °C resulted in the formation of BC5 nanoplates having larger and smooth edges with an average thickness of ~15 nm. The observed morphological transformations align with previous studies indicating that crystallite size increases with higher calcination temperatures.[39]

The TEM micrograph of the BC5 photocatalyst presented in Fig. 4a reveals well-defined 2D nanoplates with irregular stacking, a feature also observed through FESEM. A magnified TEM micrograph in Fig. 4b, captured from the area marked in Fig. 4a, further highlights the nanoplate's irregular shape. The SAED pattern (inset of Fig. 4b) exhibits bright diffraction spots, corresponding to the (0012) and (200) planes of tetragonal $Bi_{12}O_{17}Br_2$. The high-resolution TEM micrograph in Fig. 4c displays lattice fringes with an interplanar spacing of 3.08 Å, corresponding to the (117) plane of $Bi_{12}O_{17}Br_2$, in agreement with the XRD results. A dark field micrograph of BC5 using the HAADF mode is shown in Fig. 4d, with the corresponding elemental maps for Bi, Br, and O presented in Fig. 4e, f and g, respectively. Notably, the intensity of Br (Fig. 4f) in the elemental map appears to be significantly lower compared to those of Bi and O. This disparity arises from the stoichiometric composition of the BC5 ($Bi_{12}O_{17}Br_2$) photocatalyst, where the bromine content is inherently lower relative to bismuth and oxygen. Also, this further confirms the bromine loss due to calcination at higher temperatures.

The BET surface area and pore characteristics of the synthesized samples (BOB, BC2, BC3, BC4 and BC5) were determined from N_2 adsorption–desorption isotherms (Fig. S4). All samples exhibited type IV isotherms with H3 hysteresis loops (according to the BDDT classification), characteristic of slit-like mesopores commonly associated with plate-like morphologies.[27] The corresponding surface area, pore diameter, and pore volume are summarized in Table S5. A progressive decrease in surface area with increasing calcination temperature was observed, attributable to enhanced crystallinity and particle agglomeration, in agreement with FESEM/TEM observations.[40,41] In contrast, the average pore diameter increased with calcination, likely due to the coalescence or collapse of smaller pores into larger mesopores during thermal treatment. These mesostructural features are expected to facilitate improved mass transport and rapid diffusion of reactants and intermediates, while also providing accessible surface-active sites such as hydroxyl groups and adsorbed water molecules.[42–44] Such characteristics are beneficial for photocatalytic reactions, although surface area and porosity alone may not fully explain activity trends and must be considered in conjunction with crystallinity, morphology, and defect chemistry.

3.2. Optical characterization

The optical properties and bandgap energy values of the synthesized photocatalysts were analyzed using UV-vis DRS. The phase transitions induced by calcination at different temperatures had a notable impact on the optical characteristics of the $Bi_xO_yBr_z$ photocatalysts, which in turn influenced their photocatalytic efficiency.[45] Color photographs of the synthesized photocatalysts, presented alongside their UV-vis DRS spectra (Fig. 5), illustrate a visible color variation correlating with the absorption edge shift. As shown in Fig. 5a, the absorption edges for BC2, BC3, BC4, and BC5 are approximately 410 nm, 500 nm, 490 nm and 505 nm, respectively, indicating a progressive red shift. This shift corresponds to a gradual color change from white to varying shades of yellow.

The bandgap energy (E_g) was determined using the Tauc plot method in conjunction with the Kubelka–Munk function,

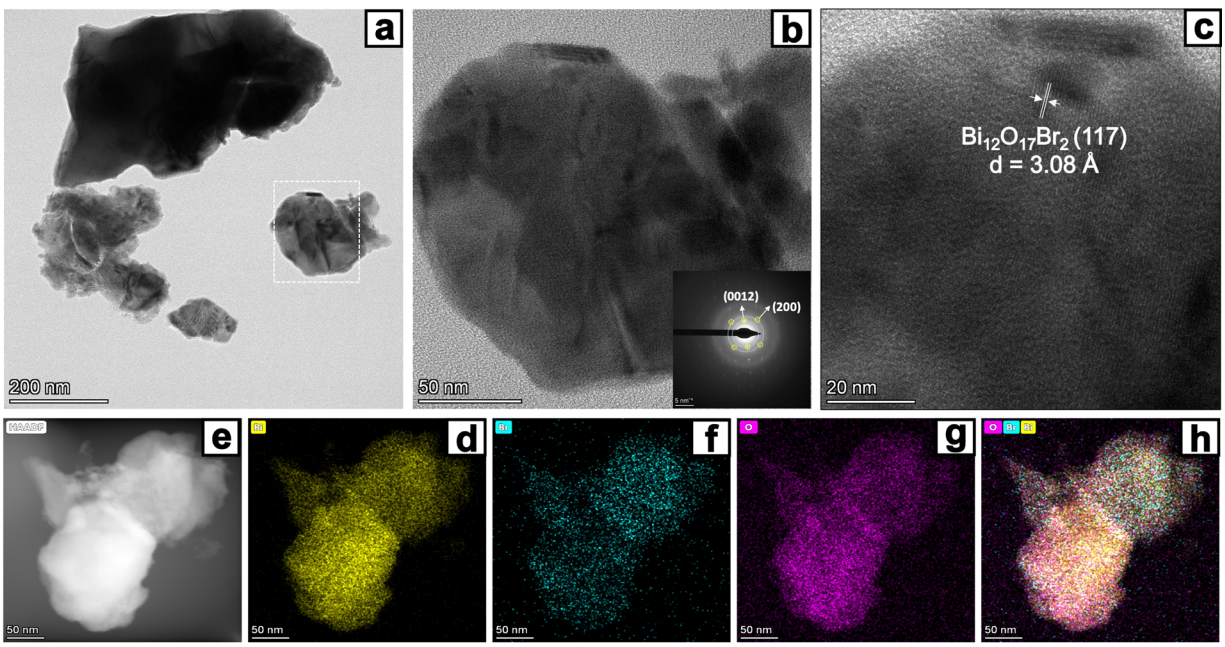

Fig. 4 (a) TEM micrograph of $Bi_{12}O_{17}Br_2$ (BC5) showing its nanoplate-like morphology, (b) magnified TEM micrograph of an individual nanoplate captured from the area marked in (a), (c) HRTEM micrograph of the top portion of the nanoplate shown in (b), (d) HAADF micrograph of $Bi_{12}O_{17}Br_2$, (e–g) elemental maps corresponding to Bi, Br, and O, respectively, and (h) composite elemental map illustrating the spatial distribution and interaction of Bi, Br and O. The inset in (b) presents the SAED pattern of $Bi_{12}O_{17}Br_2$.

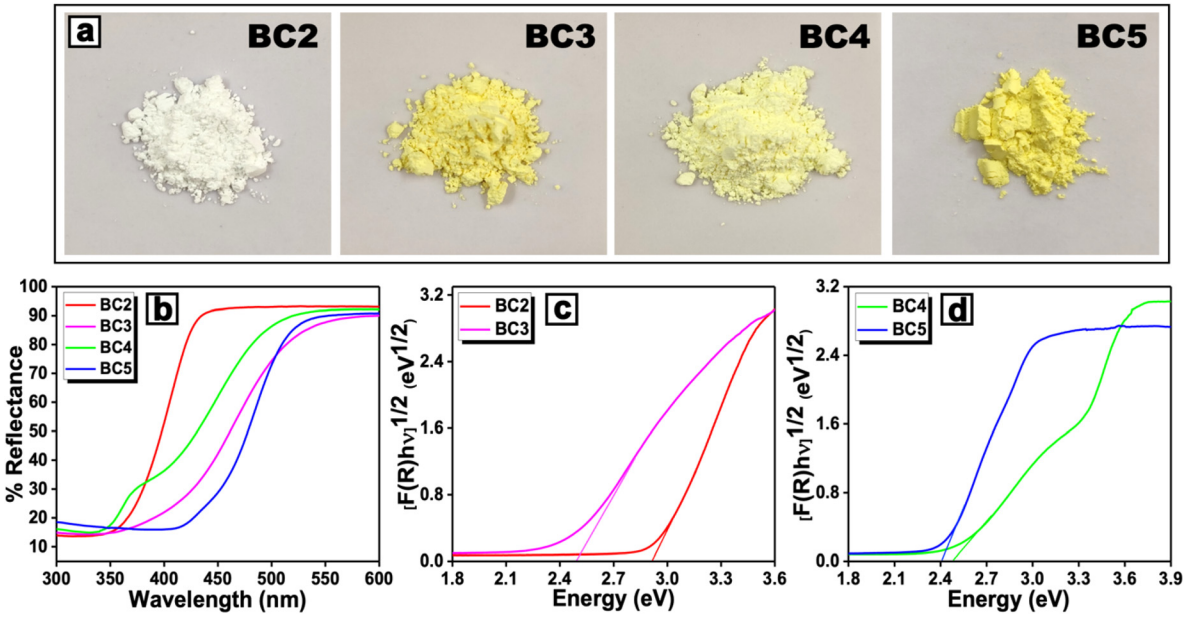

Fig. 5 (a) Photographs of the as-synthesized $Bi_xO_yBr_z$ photocatalysts, (b) UV-vis diffuse reflectance spectra of the BC2, BC3, BC4, and BC5 photocatalysts, along with the corresponding Tauc plots for (c) BC2 and BC3 and (d) BC4 and BC5. The effective bandgaps of the photocatalysts are estimated from the *x*-axis intercepts of the extrapolated dashed lines in the Tauc plots.

a well-established approach for indirect semiconductors such as BiOBr.[46] A plot of photon energy ($h\nu$) *versus* $[h\nu F(R)]^{1/2}$ was generated, and the E_g values were estimated by extrapolating the linear region of the graph to the *x*-axis, as shown in Fig. 5b and c. A detailed explanation regarding the Tauc plot method including the conversion of reflectance data using the Kubelka–Munk function and the extrapolation procedure used to determine E_g, is provided in Text S3 (SI).[46] The calculated E_g values for BC2, BC3, BC4, and BC5 were 2.91, 2.49, 2.47, and 2.40 eV, respectively.

XRD analysis confirmed the increase in crystallite size with higher calcination temperatures. This increase in crystallite size was accompanied by a red shift in the absorption edge and a reduction in E_g values. Such behavior can be attributed to quantum size effects in semiconductors, where larger crystallite sizes typically result in decreased E_g.[47,48] The valence band energy levels (E_{VB}) for BC2, BC3, BC4, and BC5 were estimated using the equation $E_{VB} = X - E_e + 0.5E_g$, where X represents the absolute electronegativity of the material, and E_e is the energy of free electrons on the hydrogen scale (approximately 4.5 eV). The conduction band energy levels (E_{CB}) were subsequently determined using $E_{CB} = E_{VB} - E_g$, with the computed values summarized in Table S2 (SI).[4]

Photoluminescence (PL) spectroscopy was employed to investigate charge carrier dynamics and recombination behavior in the synthesized photocatalysts.[49] A strong PL signal generally indicates rapid exciton recombination, while a weaker intensity suggests improved charge separation and reduced recombination losses.[50] Fig. 6 presents the PL emission spectra of the photocatalysts, recorded within the 400–600 nm wavelength range using an excitation wavelength of 350 nm.

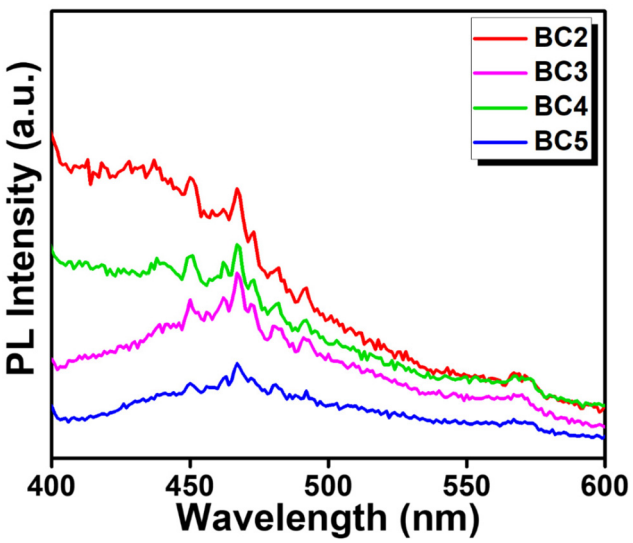

Fig. 6 Photoluminescence spectra of the BC2, BC3, BC4, and BC5 photocatalysts.

All samples exhibited an emission peak near 470 nm. Notably, the PL intensity decreased as the calcination temperature increased, suggesting enhanced crystallinity and reduced structural defects, which in turn minimized charge carrier recombination.[51] Among the synthesized photocatalysts, BC5 exhibited the weakest PL intensity, indicating superior charge separation efficiency and an extended carrier lifetime. In contrast, BC2 displayed the highest PL intensity, suggesting a higher rate of recombination.

3.3. Visible light driven photodegradation of MB dye and acetaminophen

The photocatalytic performance of the synthesized $Bi_xO_yBr_z$ photocatalysts was first assessed by monitoring the degradation of MBD (10 ppm) under visible light irradiation. The corresponding UV-vis absorption spectra for BOB, BC2, BC3, BC4, and BC5 are shown in Fig. S5(a–e). A gradual decrease in the intensity of the characteristic MBD absorption peak at λ_{max} = 665 nm reflects the progressive degradation of the dye. In the dark, adsorption experiments revealed decreases in MBD absorbance of 52%, 42%, 25%, 13% and 12% for BOB, BC2, BC3, BC4, and BC5, respectively (Fig. S5a–f), indicating that BOB had the highest adsorption capacity, followed by BC2. Upon subsequent visible light irradiation (Fig. S5f), the degradation efficiency exceeded 90% within 90 min for BOB, BC2 and BC5, whereas BC3 and BC4 showed comparatively lower efficiencies of 72% and 76%. Although BC2 exhibited a higher adsorption capacity than BC5, both catalysts achieved efficient MBD degradation under illumination. Kinetic analysis (Fig. S5g) revealed apparent reaction rate constants (k) of 0.0435 min^{-1} for BC2 and 0.0244 min^{-1} for BC5, demonstrating that BC2 promoted a reaction rate more than twice as fast as BC5.

To further assess photocatalyst stability, the degradation of 10 ppm AMP was performed under identical conditions (Fig. S6a–e). In this experiment, BOB showed relatively low activity, whereas BC2 exhibited an unusual increase in absorbance during the reaction. Both BOB and BC2 underwent pronounced photocorrosion, as evidenced by a distinct color change of the suspension from white to black (Fig. S7). To determine whether this photocorrosion was triggered specifically by AMP, additional photocatalytic tests were carried out in CIP (ciprofloxacin) and in pure DI water (pollutant-free control). Notably, similar color changes were observed in both CIP (Fig. S8a and b) and DI water (Fig. S8c and d), confirming that the instability of BOB and BC2 arises from their intrinsic susceptibility to photocorrosion rather than from any reducing action of AMP. Post-reaction XRD analysis of BC2 (BC2AR, Fig. S9a) revealed an additional peak at 2θ = 33.49°, corresponding to metallic Bi, consistent with $Bi^{3+} \rightarrow Bi^0$ photoreduction.[52] Such photocorrosion – likely driven by structural defects or incomplete phase transformation – renders BOB and BC2 unsuitable for long-term photocatalytic use under visible light.[53] In contrast, the fully transformed $Bi_xO_yX_z$ phases (BC3, BC4, and BC5) exhibited no visible color change after photocatalysis. To further confirm the structural stability, post-photocatalytic XRD analysis was performed on BC3, BC4, and BC5 following AMP degradation. As shown in Fig. S9(b–d), the diffraction patterns of all three samples remained unchanged, with no additional peaks corresponding to metallic Bi^0 (typically observed near $2\theta \approx 27°$ and 33°). These results demonstrate that the non-stoichiometric Bi-rich phases do not undergo $Bi^{3+} \rightarrow Bi^0$ photoreduction under visible-light irradiation, confirming their superior structural and electronic stability.[11] Photodegradation plots (Fig. S6c–e) showed minimal AMP adsorption (<10%) on BC3–BC5. Among them, BC5 demonstrated the highest activity, achieving ~96% degradation within 120 min under visible light (Fig. 7a). This enhanced performance can be linked to XPS analysis, which revealed a reduced Br 3d signal intensity after calcination. The loss of bromine suggests volatilization at high temperatures, creating Br-related surface vacancies that act as electron traps, improve charge separation, and promote ROS generation. By contrast, the lower efficiencies of BC3 and BC4 may arise from their smaller crystallite size, which increases recombination centers.[38,54] A comparison of the photocatalytic activity of $Bi_{12}O_{17}Br_2$ synthesized *via* methods other than calcination, as reported in the literature and summarized in Table S4 (SI), clearly indicates the superior performance of the present BC5

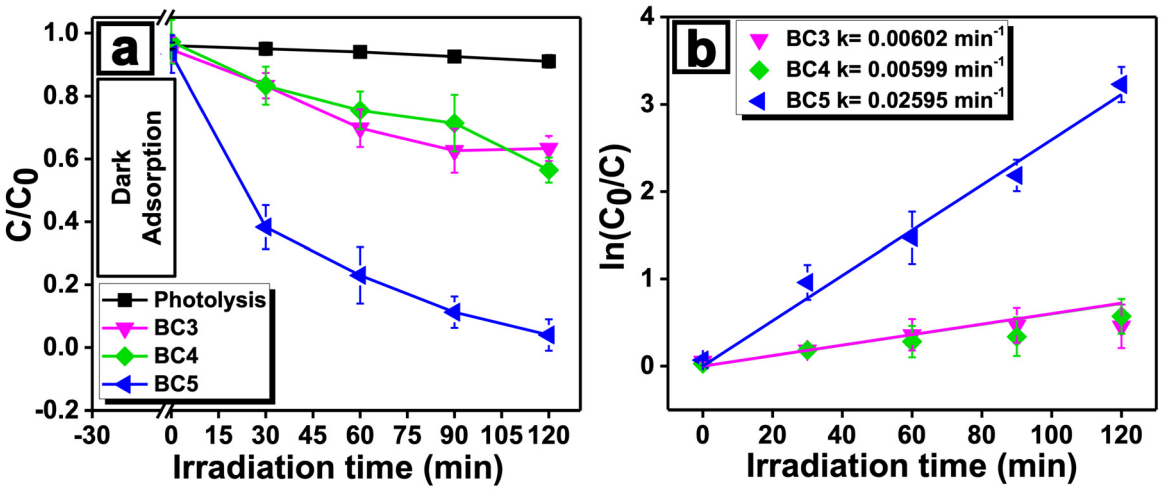

Fig. 7 (a) Time-dependent photocatalytic degradation of 10 ppm AMP under visible light irradiation in the presence of the $Bi_4O_5Br_2$ (BC3), $Bi_5O_7Br_2$ (BC4), and $Bi_{12}O_{17}Br_2$ (BC5) photocatalysts, and (b) the corresponding pseudo-first-order kinetics plots. The rate constants determined from the plots are provided in the inset.

sample. Furthermore, a comparative analysis of the reported $Bi_{12}O_{17}Br_2$-based heterojunction photocatalysts prepared using non-calcination routes (Table S4) demonstrates that the BC5 photocatalyst synthesized in this work *via* a cost-effective approach exhibits competitive – and in several cases superior – photocatalytic activity toward the degradation of emerging organic pollutants. While many Bi-based photocatalysts are typically synthesized *via* hydrothermal or multi-step fabrication strategies with greater complexity, the BC5 photocatalyst prepared here through a simple precipitation–calcination route offers a more practical and scalable alternative without compromising degradation efficiency.[55,56]

A plot of $\ln(C_0/C)$ *versus* irradiation time (Fig. 7b) shows a linear fit, confirming pseudo-first-order kinetics for AMP degradation. The rate constant (k) was the highest for BC5 (0.0261 min^{-1}), far exceeding those of BC3 (0.0047 min^{-1}) and BC4 (0.0045 min^{-1}), indicating superior photocatalytic efficiency. HPLC chromatograms (Fig. S10) further tracked AMP degradation with BC5, showing a steady decline in the AMP peak at 5.49 min (see Table S5) and the appearance of new peaks at 7–8 min, attributed to degradation by-products.[57] After 120 min, both AMP and its intermediates showed markedly reduced intensities, confirming effective breakdown and mineralization.

To identify these by-products, LC-MS analysis was performed. The observed m/z values allowed assignment of key intermediates and proposal of degradation pathways (Fig. S12). Hydroxyl radicals ($^{\bullet}OH$), identified as the dominant reactive oxygen species from scavenger studies (Section 3.6), were the principal oxidants, consistent with the literature.[57,58] LC-MS spectra revealed protonated AMP at m/z 152 (Fig. S11a). In Pathway I, $^{\bullet}OH$ attack produced *p*-aminophenol (m/z 108), which oxidized to *p*-nitrophenol (m/z 139) and subsequently to 1,4-hydroquinone (m/z 110).[57,59,60] Pathway II involved *N*-acetyl-*p*-benzoquinone imine (NAPQI, m/z 147), a known toxic metabolite, which further oxidized to 1,4-hydroquinone.[59,61,62] Pathway III included $^{\bullet}OH$ attack at the *para*-position, forming an *N*-(1,4-dihydroxyphenyl)acetamide radical that degraded to 1,4-hydroquinone and acetamide.[63] Across all pathways, 1,4-hydroquinone emerged as a central intermediate, eventually oxidizing to benzoic acid (m/z 122, Fig. S11d) and hexenoic acid (m/z 113), before complete mineralization into CO_2 and H_2O.[64] The new HPLC peak at 7–8 min is thus assigned to benzoic acid.[57] These findings highlight BC5 as the most efficient photocatalyst among the series, underscoring its potential for environmental remediation.

3.4. Photocatalytic degradation of algal cells and detailed analysis

The BC5 photocatalyst, identified as the most efficient among the synthesized samples, was used to evaluate its ability to degrade MA under visible light irradiation. The photodegradation of the algal cells was analyzed through key biological markers, including chlorophyll-a concentration, malondialdehyde (MDA) content, and electrolytic leakage (EL). Chlorophyll-a is a crucial indicator of algal growth, as its concentration per unit volume reflects photosynthetic activity, cell density, and biomass accumulation.[65] A reduction in chlorophyll-a levels signifies declining photosynthetic efficiency and increased cellular stress.[66] Therefore, photocatalytic degradation under visible light was assessed by tracking chlorophyll-a concentrations through optical density measurements.

As shown in Fig. 8a, the BC5 photocatalyst significantly reduced chlorophyll-a levels compared to the control sample. After 120 min of visible light irradiation, the chlorophyll-a concentration decreased from 3.88 μg ml^{-1} to 0.15 μg ml^{-1}, achieving an impressive degradation efficiency of 96% as shown in Fig. 8b. Lipid peroxidation, induced by oxidative stress from ROS such as hydroxyl radicals ($^{\bullet}OH$) and superoxide radicals ($^{\bullet}O_2^-$) generated during the photocatalysis, primarily affects the algal cell membrane, leading to structural damage and intracellular leakage.[65,67,68] The process is initiated by the abstraction of hydrogen atoms from unsaturated phospholipid chains, resulting in the formation of lipid hydroperoxides, which subsequently degrade into MDA.[69]

The extent of lipid peroxidation in MA subjected to photocatalysis in the presence of BC5 was assessed at different time intervals (0 min, 60 min, and 120 min) and compared with a control sample (Fig. 8c). Initially, the MDA concentration was measured at 1.93 nmol ml^{-1}. Following the dark adsorption phase with BC5, the MDA levels increased to 4.84 nmol ml^{-1}. Notably, after 120 min of visible light exposure, the MDA concentration rose significantly to 9.68 nmol ml^{-1}. The progressive rise in MDA levels suggests severe oxidative damage in MA exposed to ROS.[5] This oxidative stress disrupts entire cellular functions by altering membrane permeability, impairing ion channels, and ultimately leading to membrane disintegration. The sharp rise in MDA concentration confirms effective algal cell degradation *via* photocatalysis. Additionally, the EL was measured to assess stress tolerance in algal cells experiencing membrane damage.[70] As illustrated in Fig. 8d, the initial EL percentage in MA before photocatalysis was 64%. However, after 120 min of treatment under visible light in the presence of BC5, the EL increased significantly to 88.87%. A continuous rise in EL with increasing irradiation time further confirms the ability of BC5 to disrupt algal cell membranes and facilitate degradation. A summary of chlorophyll-a concentration, MDA content, and EL percentage values recorded during the photodegradation of MA is provided in Table S6 (SI).

3.5. Validation of algal cell rupture through fluorescence microscopy

The efficacy of BC5 in disrupting algal cells was further confirmed using epi-fluorescence microscopy,[71] capturing structural variations in MA colonies over time, as illustrated in Fig. 9. Bright-field and fluorescence images were taken at different time intervals: 0 min (dark phase), 60 min, and 120 min using the aliquots of MA collected during the visible-light-driven photodegradation with BC5 as the photocatalyst. The fluorescence images in Fig. 9b show bright red fluorescence, indicating the presence of intact, viable algal cells with a high chlorophyll-a content. The bright-field microscopy confirmed the characteristic spherical morphology of MA

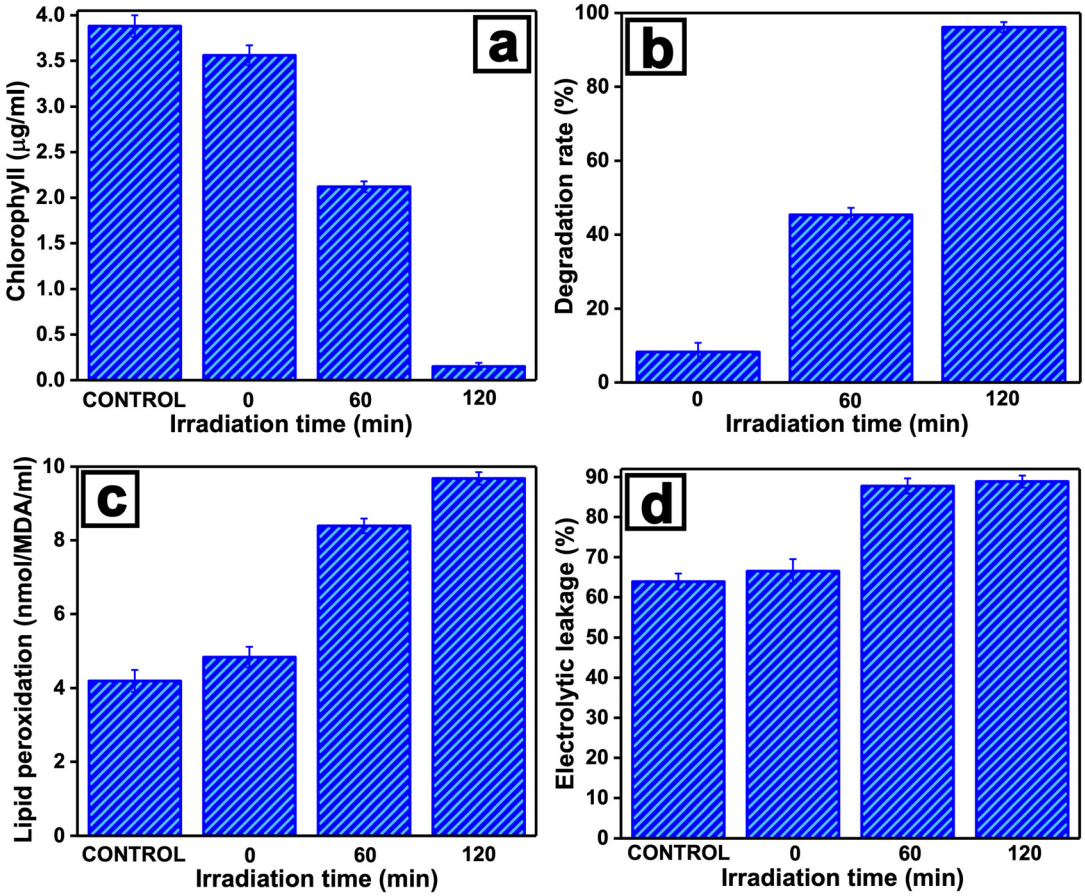

Fig. 8 Graphs illustrating variations in key biological markers during the visible-light-induced photodegradation of *M. aeruginosa* cells in the presence of BC5 as the photocatalyst: (a) changes in chlorophyll-a concentration, (b) the corresponding photodegradation rates based on chlorophyll-a reduction, (c) lipid peroxidation levels, and (d) electrolytic leakage.

before exposure to the photocatalyst, which corresponded to strong fluorescence intensity (Fig. 9a).

During the 30 min dark adsorption phase, no significant morphological alterations were observed in the algal cells (Fig. 9c and d), confirming that BC5 alone did not cause any noticeable damage in the absence of light. However, after 60 min of visible light irradiation, minor structural changes and reduced fluorescence intensity were observed (Fig. 9e and f), suggesting a decline in chlorophyll-a concentration. By 120 min, the algal cells displayed evident rupture, with fluorescence images revealing a shift in color from red to green (Fig. 9g and h), indicating complete chlorophyll-a degradation. These microscopic observations align with the chlorophyll reduction trends discussed in the previous section. Moreover, the chlorophyll-a content remained undetectable (0 mg ml^{-1}) even after 5 days of incubation under optimal conditions (details of algal cell regrowth experiments are provided in the SI, S6). This confirms that the algal cells underwent complete rupture due to BC5-induced photodegradation under visible light, effectively preventing regrowth.

To further validate that the observed inactivation of algal blooms is primarily due to photocatalytic activity, a control experiment was conducted by exposing *Microcystis aeruginosa* algae-containing water to visible light in the absence of any catalyst for 1 h. A minor visual change in color from dark to light green was observed; however, quantitative analysis of chlorophyll-a content based on optical density measurements showed a slight increase from 0.302 μg mL^{-1} to 0.318 μg mL^{-1} after 1 h of light exposure, indicating continued algal growth under these conditions.

3.6. Role of reactive species through scavenger studies and Mott–Schottky analysis

As noted in Section 3.3, BC2 exhibited comparable efficiency to BC5 in degrading MBD; however, BC2 underwent photocorrosion during AMP degradation. This was evident from the reaction solution turning black (see Fig. S7d), indicating the reduction of Bi^{3+} to metallic Bi^0 (see Fig. S9). The selective degradation behavior can be attributed to the interaction between the pollutants and the photocatalyst, particularly the electron-donating groups in AMP, which can reduce the unstable BiOBr phase in BC2. In contrast, BC3, BC4, and BC5 remained stable due to their non-stoichiometric $Bi_xO_yBr_z$ composition.[52,72]

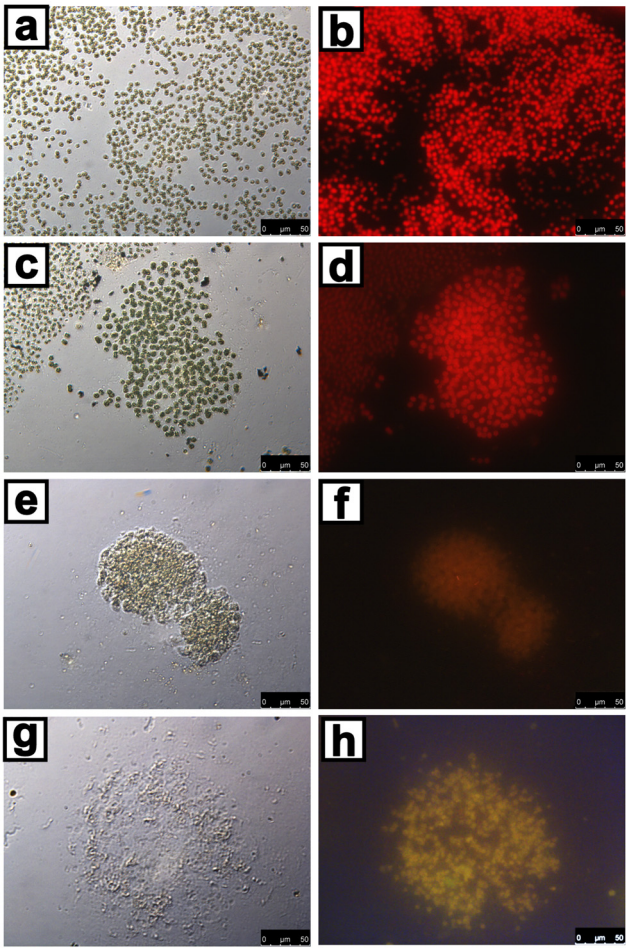

Fig. 9 Microscopic examination of *M. aeruginosa* cells before and after visible-light-induced photodegradation using BC5 as the photocatalyst. Bright field images are shown in (a), (c), (e) and (g), while the corresponding fluorescence images are in (b), (d), (f) and (h). The images represent control samples (a and b), post-dark phase samples (30 min of stirring in the dark) at 0 min (c and d), samples following 60 min of irradiation (e and f), and samples after 120 min of irradiation (g and h).

The role of different ROS in the degradation process was further analyzed using scavenger studies. Specific scavengers, including hydroquinone (HQ) for $^{\bullet}O_2^-$, ammonium oxalate (AO) for h^+, potassium dichromate ($K_2Cr_2O_7$) for e^-, and isopropanol (IPA) for $^{\bullet}OH$, were added to AMP solutions before reaction with BC5. As shown in Fig. S14, the presence of $K_2Cr_2O_7$ significantly reduced the degradation efficiency of BC5 from 96% to 15%, followed by IPA (34%), AO (61.3%), and HQ (91.3%), indicating that e^- and $^{\bullet}OH$ were the primary reactive species in AMP degradation. The generation of ROS depends on the band edge positions of the photocatalysts, which were determined using Mott–Schottky analysis and Tauc plot analysis. The estimated valence and conduction band edge potentials of BC2, BC3, BC4, and BC5, calculated using Kubelka–Munk theory, are presented in Table S3. These values were experimentally validated through Mott–Schottky analysis (Fig. 10a–d). The flat-band potentials were referenced to pH = 7 and converted to the NHE scale accordingly. Full experimental details, including the electrode preparation and measurement conditions, are provided in Text S4 (SI).[73]

The positive slopes in the Mott–Schottky ($1/C^2$ *vs.* potential) plots confirm that all $Bi_xO_yBr_z$ samples exhibit n-type semiconducting behavior. The flat-band potentials from these plots were −0.39, −0.36, −0.38, and −0.32 V *vs.* Ag/AgCl for BC2, BC3, BC4, and BC5, respectively. After converting to the normal hydrogen electrode scale using the relation $E_{NHE} = E_{Ag/AgCl} + 0.198$ V, the corresponding values are −0.19, −0.16, −0.18, and −0.12 *vs.* NHE. Because the flat-band potential of an n-type semiconductor lies approximately 0.1 V above the conduction band (CB) edge, the estimated CB positions are −0.29, −0.26, −0.28, and −0.22 V *vs.* NHE for BC2, BC3, BC4, and BC5, respectively. Using $E_{VB} = E_{CB} + E_g$, the calculated VB edge positions are 2.6, 2.22, 2.18, and 2.17 V for BC2–BC5. A schematic summarizing these band positions is shown in Fig. 10e.

These values indicate that the CB of BC5 (−0.22 V *vs.* NHE) is insufficiently negative to reduce O_2 to $^{\bullet}O_2^-$ ($O_2/^{\bullet}O_2^-$ = −0.33 V *vs.* NHE),[11] whereas its VB (2.17 V) is strongly positive enough to oxidize surface OH^- to $^{\bullet}OH$ ($OH^-/^{\bullet}OH$ = 1.99 V, $H_2O/^{\bullet}OH$ = 2.27 V *vs.* NHE).[74] Thus, BC5 predominantly generates e^- and $^{\bullet}OH$ as the major reactive species, while the $^{\bullet}O_2^-$ formation is thermodynamically limited. This is fully consistent with the results of AMP scavenger studies (Fig. S14), which identified e^- and $^{\bullet}OH$ as the dominant ROS and showed only a minor contribution from $^{\bullet}O_2^-$.

For MBD degradation, BC2 exhibits higher photocatalytic efficiency than BC5, attributable to its significantly more positive VB (2.60 V). This VB position is well above the potential required to generate $^{\bullet}OH$ from both OH^- and H_2O, enabling BC2 to produce a higher density of oxidative $^{\bullet}OH$ radicals. Because MBD possesses a conjugated chromophore highly susceptible to $^{\bullet}OH$ and $^{\bullet}O_2^-$-driven oxidative cleavage, the enhanced $^{\bullet}OH$ generation capability of BC2 results in superior degradation performance. The scavenger experiments (Fig. S13) corroborate this: addition of IPA ($^{\bullet}OH$ scavenger) suppressed the MBD degradation by 95% for BC2 and 84% for BC5, confirming that $^{\bullet}OH$ is the primary oxidant in both cases. For MA degradation using BC5, ROS quenching decreased the efficiency from 96% to 59% ($^{\bullet}OH$ scavenger), 62% (e^- scavenger), 63% (h^+ scavenger), and 71% ($^{\bullet}O_2^-$ scavenger) (Fig. S15). These results again indicate the predominance of $^{\bullet}OH$, with secondary contributions from e^- and h^+. Overall, these band-structure and scavenger analyses demonstrate that $^{\bullet}OH$ radicals are the primary ROS driving both MBD and MA degradation, whereas e^- (with supporting $^{\bullet}OH$) dominates AMP degradation when BC5 is employed as the photocatalyst. Although electron paramagnetic resonance (EPR) spectroscopy is the most direct and definitive technique for identifying short-lived ROS, we were unable to perform EPR analysis for the present work. Nevertheless, we have additionally confirmed the molecular fingerprint of $^{\bullet}OH$ during AMP degradation from LC-MS data as discussed in Text S8 (SI).

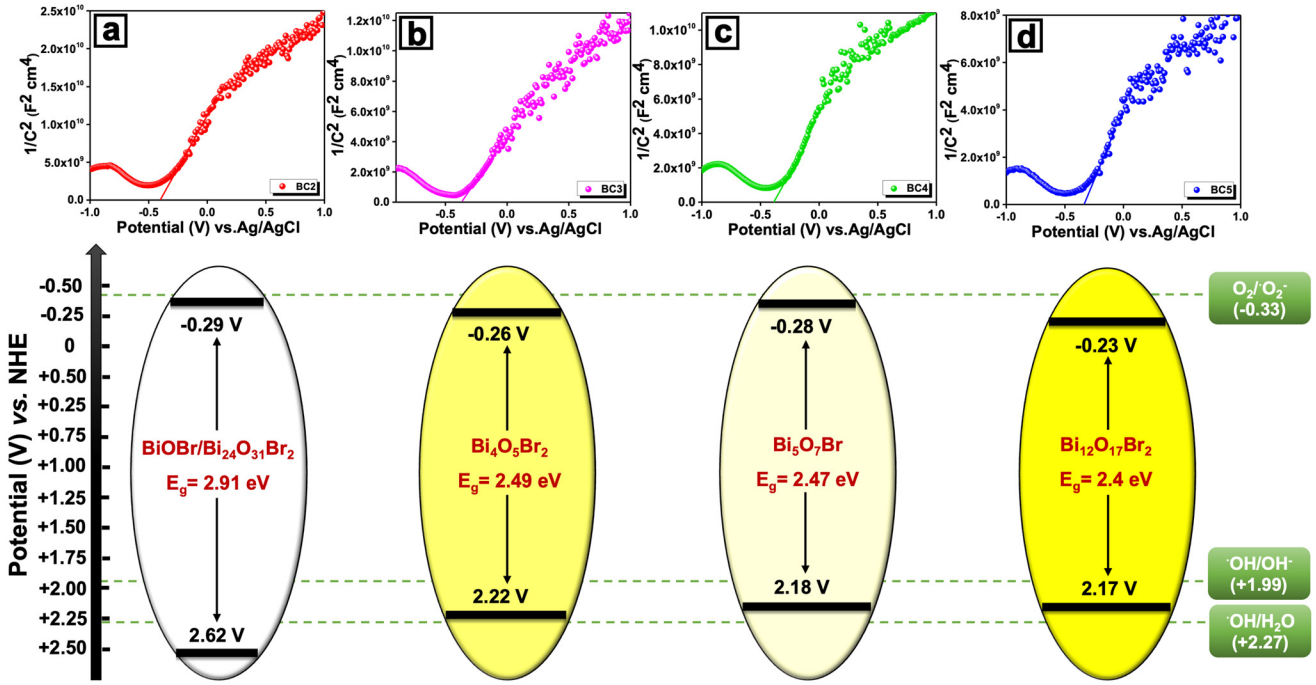

Fig. 10 Mott–Schottky plots for (a) BC2, (b) BC3, (c) BC4, and (d) BC5, illustrating their flat band potentials. (e) A schematic representation of the conduction and valence band positions of the synthesized $Bi_xO_yBr_z$ photocatalysts relative to the standard hydrogen electrode potential, as determined from the Mott–Schottky analysis.

3.7. Correlation of phase transformation, defect chemistry, and photocatalytic activity

The progressive phase transformations observed in the $Bi_xO_yBr_z$ series upon calcination play a decisive role in determining the photocatalytic activity, as each phase possesses a distinct electronic configuration, defect density, and a halide coordination environment that collectively govern charge separation and ROS formation. The low-temperature phases ($Bi_{24}O_{31}Br_{10}$ and $Bi_4O_5Br_2$) retain a relatively high Br content and exhibit limited oxygen-vacancy formation, resulting in wider bandgaps and less efficient visible-light harvesting. As the calcination temperature increases, the transformation into Bi_5O_7Br introduces a higher concentration of lattice oxygen defects, which serve as shallow donor states enhancing charge carrier mobility; however, the layered configuration still restricts interlayer charge transport. Further calcination yields highly oxygen-deficient $Bi_{12}O_{17}Br_2$ (BC5), whose mixed-valence Bi–O framework and reduced Br content synergistically promote stronger internal electric fields and improved orbital hybridization between Bi 6s, O 2p, and Br 4p states. These features markedly enhance spatial charge separation and extend the lifetime of photogenerated electrons and holes. The attenuated Br 3d signal observed in XPS for BC5 is consistent with partial Br volatilization and concomitant formation of oxygen vacancies, which serve as active sites for O_2 adsorption and its subsequent reduction to $^{\bullet}O_2^-$, while also facilitating hole-mediated $^{\bullet}OH$ generation. These structural–electronic attributes explain why BC5 exhibits the highest rates of MB, acetaminophen, and algal cell degradation: the enhanced vacancy-mediated activation of molecular oxygen and the more favorable band-edge positions of $Bi_{12}O_{17}Br_2$ collectively maximize ROS production under visible light. Thus, the superior photocatalytic ability of BC5 directly arises from the thermally driven evolution of phase composition, vacancy concentration, and electronic structure across the $Bi_xO_yBr_z$ series.

4. Conclusion

A series of bismuth-rich bismuth oxybromide photocatalysts were synthesized by chemical precipitation followed by controlled calcination. The calcination temperature governed the phase evolution from BiOBr through $Bi_{24}O_{31}Br_{10}$, $Bi_4O_5Br_2$, Bi_5O_7Br, and $Bi_{12}O_{17}Br_2$, as confirmed by XRD, XPS, FESEM, and TEM. This phase evolution correlates strongly with photocatalytic activity, underscoring the central role of structural transformations in tuning the performance. These materials display a distinctive 2D nanoplate morphology. Among the series, $Bi_{12}O_{17}Br_2$ (BC5) showed the highest activity under visible-light irradiation for acetaminophen degradation, consistent with HPLC/LC-MS analysis. Its superior performance is attributed to high crystallinity and bromine-vacancy defects generated upon calcination – evidenced by the decreased Br 3d XPS signal – which together optimize the band structure, promote charge separation, and enhance ROS formation. Scavenger studies indicate that electrons and hydroxyl radicals are the primary oxidants in

acetaminophen degradation. BC5 also exhibited excellent performance against *Microcystis aeruginosa* algal cells, achieving over 96% degradation within 120 min, confirmed through decreased chlorophyll-a content, increased malondialdehyde, and elevated electrolyte leakage, indicating irreversible cell rupture. Scavenger studies identified hydroxyl radicals as the dominant species for algal cell degradation, followed by electrons, holes, and superoxide. No chlorophyll-a was detected (0 mg mL^{-1}) after five days of incubation, confirming the absence of regrowth. Overall, this work shows that calcination-driven phase transformation in bismuth-rich oxybromides suppresses photocorrosion, improves charge-carrier dynamics, and delivers durable, high-efficiency photocatalysis. The outstanding performance of BC5 toward both organic pollutants and algal cells highlights its promise for environmental remediation.

Conflicts of interest

There are no conflicts to declare.

Data availability

The data supporting this article have been included as part of the supplementary information (SI), which contains material characterization details, photocatalytic degradation studies of HABs under visible light, XRD and Williamson-Hall analyses, FESEM micrographs, BET data, bandgap estimation and electrochemical methods, UV-vis absorption spectra, kinetic analyses for methylene blue and acetaminophen degradation, photocorrosion photographs corresponding to BOB and BC2, pre- and post-reaction XRD patterns of the photocatalysts, HPLC and LC-MS analyses of acetaminophen degradation, and cyclic stability and reusability data. Supplementary information is available. See DOI: https://doi.org/10.1039/d5nr05038c.

Acknowledgements

The authors acknowledge assistance from the Central Sophisticated Instrumentation Facility (CSIF), University of Calicut, for XRD and HPLC analysis. KS acknowledges the financial support from the University Grants Commission, India through the start-up grant. AZJ acknowledges financial support from the Polish National Science Centre under grant no. UMO-2021/43/B/ST5/02983.

References

1 P. M. Rajaitha, S. Hajra, M. Sahu, K. Mistewicz, B. Toroń, R. Abolhassani, S. Panda, Y. K. Mishra and H. J. Kim, *Mater. Today Chem.*, 2022, **23**, 100692.
2 K. Liu, J. Chen, F. Sun, Y. Liu, M. Tang and Y. Yang, *Sci. Total Environ.*, 2022, **835**, 155482.
3 H. Li, B. Cheng, J. Zhang, X. Zhou, C. Shi, L. Zeng and C. Wang, *J. Environ. Chem. Eng.*, 2023, **11**, 110371.
4 S. Ghali, L. Mammeri, H. Boucheloukh and T. Sehili, *J. Photochem. Photobiol., A*, 2024, **446**, 115121.
5 G. Fan, X. Lin, Y. You, B. Du, X. Li and J. Luo, *J. Hazard. Mater.*, 2022, **421**, 126703.
6 G. Xie, X. Hu, Y. Du, Q. Jin, Y. Liu, C. Tang, X. Hu, G. Li, Z. Chen, D. Zhou and H. Wang, *Chem. Eng. J.*, 2021, **417**, 129244.
7 K. Sridharan, E. Jang and T. J. Park, *CrystEngComm*, 2013, **15**, 8241–8245.
8 S. Shenoy and K. Sridharan, *Surf. Interfaces*, 2022, 101941.
9 K. Sridharan and T. J. Park, *Appl. Catal., B*, 2013, **134**, 174–184.
10 Z. S. Liu, H. S. Ran, J. N. Niu, P. Z. Feng and Y. B. Zhu, *J. Colloid Interface Sci.*, 2014, **431**, 187–193.
11 K. Sridharan, S. Shenoy, S. G. Kumar, C. Terashima, A. Fujishima and S. Pitchaimuthu, *Catalysts*, 2021, **11**, 426.
12 A. Chachvalvutikul, T. Luangwanta, B. Inceesungvorn and S. Kaowphong, *J. Colloid Interface Sci.*, 2023, **641**, 595–609.
13 Y. Mi, H. Li, Y. Zhang and W. Hou, *J. Colloid Interface Sci.*, 2019, **534**, 301–311.
14 X. Jin, L. Ye, H. Xie and G. Chen, *Coord. Chem. Rev.*, 2017, **349**, 84–101.
15 K. L. Zhang, C. M. Liu, F. Q. Huang, C. Zheng and W. D. Wang, *Appl. Catal., B*, 2006, **68**, 125–129.
16 L. Xinping, H. Tao, H. Fuqiang, W. Wendeng and S. Jianlin, *J. Phys. Chem. B*, 2006, **110**, 24629–24634.
17 E. Johnson, A. Raj, S. Kottarathil, A. Johansson and K. Sridharan, *Sep. Purif. Technol.*, 2025, **364**, 132521.
18 P. Wu, L. Feng, Y. Liang, X. Zhang, X. Li, S. Tian, H. Hu, G. Yin and S. Khan, *J. Mater. Sci.: Mater. Electron.*, 2020, **31**, 5385–5401.
19 X. Xiao, C. Liu, R. Hu, X. Zuo, J. Nan, L. Li and L. Wang, *J. Mater. Chem.*, 2012, **22**, 22840–22843.
20 C. Yue, Y. Lin, J. Sang, Z. Li, P. Zhang, M. Fan, Y. Leng, P. Jiang and A. Haryono, *Mater. Today Commun.*, 2022, **31**, 103270.
21 M. Lu, X. Xiao, Y. Xiao, J. Li and F. Zhang, *J. Colloid Interface Sci.*, 2022, **625**, 664–679.
22 K. L. Li, W. W. Lee, C. S. Lu, Y. M. Dai, S. Y. Chou, H. L. Chen, H. P. Lin and C. C. Chen, *J. Taiwan Inst. Chem. Eng.*, 2014, **45**, 2688–2697.
23 X. Xiao, C. Xing, G. He, X. Zuo, J. Nan and L. Wang, *Appl. Catal., B*, 2014, **148–149**, 154–163.
24 J. Di, J. Xia, M. Ji, S. Yin, H. Li, H. Xu, Q. Zhang and H. Li, *J. Mater. Chem. A*, 2015, **3**, 15108–15118.
25 H. L. Chen, W. W. Lee, W. H. Chung, H. P. Lin, Y. J. Chen, Y. R. Jiang, W. Y. Lin and C. C. Chen, *J. Taiwan Inst. Chem. Eng.*, 2014, **45**, 1892–1909.
26 L. Bao, B. Yuan and Y. Yuan, *ChemistrySelect*, 2024, **9**, e202401141.
27 S.-M. Fu, G.-S. Li, X. Wen, C.-M. Fan, J.-X. Liu, X.-C. Zhang and R. Li, *Trans. Nonferrous Met. Soc. China*, 2020, **30**, 765–773.
28 S. Humayun, M. Hayyan, Y. Alias and A. Hayyan, *Sep. Purif. Technol.*, 2021, **270**, 118730.

29 H. Huang, K. Xiao, T. Zhang, F. Dong and Y. Zhang, *Appl. Catal., B*, 2017, **203**, 879–888.
30 P. Nwaokafor, K. B. Okeoma, O. K. Echendu, A. C. Ohajianya and K. O. Egbo, *Metallogr., Microstruct., Anal.*, 2021, **10**, 727–735.
31 Z. Vasiljević, M. P. Dojčinović, J. D. Vujančević, M. Spreitzer, J. Kovač, D. Bartolić, S. Marković, I. Janković-Častvan, N. B. Tadić and M. V. Nikolić, *RSC Adv.*, 2021, **11**, 32358–32368.
32 S. A. Hassanzadeh-Tabrizi, *J. Alloys Compd.*, 2023, **968**, 171914.
33 Z. Zhong, H. J. Zhang, Y. Y. Yang, T. K. Zhang, X. H. Qu, L. Ma, H. L. Cao, Y. D. Hou and J. Lü, *ACS Catal.*, 2025, **15**, 6334–6345.
34 J. Yang, L. Xu, C. Liu and T. Xie, *Appl. Surf. Sci.*, 2014, **319**, 265–271.
35 L. Zhang, X. Yue, J. Liu, J. Feng, X. Zhang, C. Zhang, R. Li and C. Fan, *Sep. Purif. Technol.*, 2020, **231**, 115917.
36 Y. Su, C. Ding, Y. Dang, H. Wang, L. Ye, X. Jin, H. Xie and C. Liu, *Appl. Surf. Sci.*, 2015, **346**, 311–316.
37 D. Mao, S. Ding, L. Meng, Y. Dai, C. Sun, S. Yang and H. He, *Appl. Catal., B*, 2017, **207**, 153–165.
38 J. Li, Y. Yu and L. Zhang, *Nanoscale*, 2014, **6**, 8473–8488.
39 S. Dwivedi, H. C. Nayak, S. S. Parmar, R. P. Kumhar and S. Rajput, *Magnetism*, 2022, **2**, 45–55.
40 W. Cun, Z. Jincai, W. Xinming, M. Bixian, S. Guoying, P. Ping'an and F. Jiamo, *Appl. Catal., B*, 2002, **39**, 269–279.
41 F. Pellegrino, L. Pellutiè, F. Sordello, C. Minero, E. Ortel, V. D. Hodoroaba and V. Maurino, *Appl. Catal., B*, 2017, **216**, 80–87.
42 T. Peng, D. Zhao, K. Dai, W. Shi and K. Hirao, *J. Phys. Chem. B*, 2005, **109**, 4947–4952.
43 D. S. Kim, S. J. Han and S. Y. Kwak, *J. Colloid Interface Sci.*, 2007, **316**, 85–91.
44 J. Yang, L. Xu, C. Liu and T. Xie, *Appl. Surf. Sci.*, 2014, **319**, 265–271.
45 H. Cheng, Y. Huang, J. Wu, Y. Ling, L. Dong, J. Zha, M. Yu and Z. Zhu, *Mater. Res. Bull.*, 2020, **131**, 110968.
46 S. Shenoy and K. Sridharan, *Chem. Phys. Lett.*, 2020, **749**, 137435.
47 D. S. Kim, S. J. Han and S. Y. Kwak, *J. Colloid Interface Sci.*, 2007, **316**, 85–91.
48 K. Kočí, L. Obalová, L. Matějová, D. Plachá, Z. Lacný, J. Jirkovský and O. Šolcová, *Appl. Catal., B*, 2009, **89**, 494–502.
49 S. Shenoy, S. Ahmed, I. M. C. Lo, S. Singh and K. Sridharan, *Mater. Res. Bull.*, 2021, **140**, 111290.
50 S. Shenoy, E. Jang, T. J. Park, C. S. Gopinath and K. Sridharan, *Appl. Surf. Sci.*, 2019, **483**, 696–705.
51 M. Marks, H. Jeppesen, M. L. N. Nielsen, J. Kong, M. Ceccato, M. A. van der Veen, E. D. Bøjesen and N. Lock, *Small*, 2024, **2401413**, 1–14.
52 M. Wang, S. Osella, R. Brescia, Z. Liu, J. Gallego, M. Cattelan, M. Crisci, S. Agnoli and T. Gatti, *Nanoscale*, 2023, **15**, 522–531.
53 A. V. Karim, S. Krishnan and A. Shriwastav, *J. Indian Chem. Soc.*, 2022, **99**, 100480.
54 K. Kocí, I. Troppová, M. Reli, L. Matejová, M. Edelmannová, H. Drobná, L. Dubnová, A. Rokicinska, P. Kustrowski and L. Capek, *Front. Chem.*, 2018, **6**, 1–11.
55 S. Li, Y. Zhao, X. Zhang, Y. Liu, T. Liu, W. Li, Y. Hou, W. Jiang and B. Zhang, *Adv. Fiber Mater.*, 2025, **7**(6), 2032–2047.
56 P. Song, J. Du, X. Ma, Y. Shi, X. Fang, D. Liu, S. Wei, Z. Liu, Y. Cao, B. Lin, J. Di, Y. Wang, J. Cui, T. Kong, C. Gao and Y. Xiong, *EcoEnergy*, 2023, **1**, 197–206.
57 V. H. T. Thi and B. K. Lee, *Mater. Res. Bull.*, 2017, **96**, 171–182.
58 M. Qutob, M. A. Hussein, K. A. Alamry and M. Rafatullah, *RSC Adv.*, 2022, **12**, 18373–18396.
59 E. Moctezuma, E. Leyva, C. A. Aguilar, R. A. Luna and C. Montalvo, *J. Hazard. Mater.*, 2012, **243**, 130–138.
60 M. T. Yang, Y. Du, W. C. Tong, A. C. K. Yip and K. Y. A. Lin, *Chemosphere*, 2019, **226**, 924–933.
61 E. Leyva, E. Moctezuma, K. M. Baines, S. Noriega and E. Zarazua, *Curr. Org. Chem.*, 2017, **22**, 2–17.
62 M. Bedner and W. A. MacCrehan, *Environ. Sci. Technol.*, 2006, **40**, 516–522.
63 L. Yang, L. E. Yu and M. B. Ray, *Environ. Sci. Technol.*, 2009, **43**, 460–465.
64 J. Li, Q. Ye and J. Gan, *Water Res.*, 2014, **49**, 44–52.
65 K. V. Ajayan, P. J. Chaithra, K. Sridharan, P. Sruthi, E. Harikrishnan and C. C. Harilal, *Environ. Res.*, 2023, **237**, 116926.
66 A. Sharan and S. Nara, *Aquat. Toxicol.*, 2020, **224**, 105498.
67 Y. Yang, H. Chen and J. Lu, *Sci. Total Environ.*, 2023, **858**, 159640.
68 A. M. S., K. Sridharan, J. T. Puthur and O. P. Dhankher, *J. Agric. Food Chem.*, 2021, **69**, 10017–10035.
69 X. He, P. Wu, S. Wang, A. Wang, C. Wang and P. Ding, *J. Cleaner Prod.*, 2021, **289**, 125755.
70 V. Demidchik, D. Straltsova, S. S. Medvedev, G. A. Pozhvanov, A. Sokolik and V. Yurin, *J. Exp. Bot.*, 2014, **65**, 1259–1270.
71 A. Anjitha, K. Shijina, K. V. Ajayan, S. Swaminathan, I. M. C. Lo and K. Sridharan, *Environ. Sci.: Nano*, 2025, **12**, 262–275.
72 Y. Li, W. Song, W. Fu, D. C. W. Tsang and X. Yang, *Chem. Eng. J.*, 2015, **271**, 214–222.
73 Y. Liu, L. Lv, H. Feng, H. Liu and Y. Wang, *ACS Appl. Nano Mater.*, 2024, **7**, 27846–27857.
74 H. Huang, Y. He, X. Li, M. Li, C. Zeng, F. Dong, X. Du, T. Zhang and Y. Zhang, *J. Mater. Chem. A*, 2015, **3**, 24547–24556.

